ACS APPLIED BIO MATERIALS

www.acsabm.org Article

$BiVO_4@Bi_2S_3$ Heterojunction Nanorods with Enhanced Charge Separation Efficiency for Multimodal Imaging and Synergy Therapy of Tumor

Ze Wang, Shuwei Liu, Lu Wang, Haoyang Zou, Zidong Wang, Xiaoduo Tang, Wenjie Feng, Yu Chong,* Yi Liu,* Bai Yang, and Hao Zhang

Cite This: https://dx.doi.org/10.1021/acsabm.0c00573 Read Online

ABSTRACT: Despite malignant tumors being one of the most serious diseases threatening human health and living quality, exploring theranostic agents for highly effective tumor diagnosis and treatment is still full of challenges. Herein, we demonstrate the design and preparation of Tween-20-modified $BiVO_4@Bi_2S_3$ heterojunction nanorods (HNRs) for multimodal computed tomography (CT)/photoacoustic (PA) imaging and radiotherapy (RT)/radiodynamic therapy (RDT)/photothermal therapy (PTT) synergistic therapy. Benefiting from the high X-ray attenuation coefficient of Bi, $BiVO_4@Bi_2S_3$ HNRs exhibit a sensitive CT imaging capacity and radiation enhancement effect during RT. Meanwhile, the strong NIR absorption of Bi_2S_3 endows $BiVO_4@Bi_2S_3$ HNRs with an excellent PA imaging and photothermal transformation capacity. More importantly, by taking advantage of the type II band alignment between $BiVO_4$ and Bi_2S_3, an extra internal electric field is established to accelerate the separation of X-ray-induced electrons and holes in $BiVO_4@Bi_2S_3$ HNRs, resulting in the realization of highly effective X-ray-induced RDT. Because the in vitro and in vivo experiments have verified that the RT/RDT/PTT synergistic therapeutic efficacy is greatly superior to any single treatment, it is believed that our $BiVO_4@Bi_2S_3$ HNRs can be used as the multifunctional nanotheranostic platform for malignant tumor theranostics.

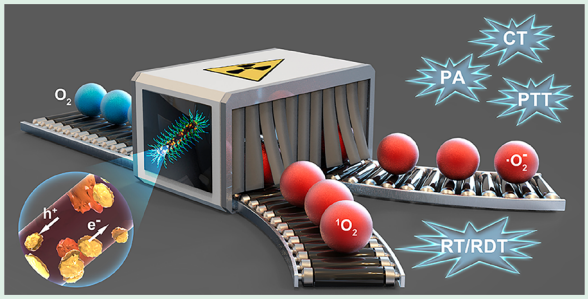

KEYWORDS: *radiosensitizers, radiodynamic therapy, $BiVO_4@Bi_2S_3$, synergistic therapy, reactive oxygen species*

1. INTRODUCTION

Over the past decades, malignant tumors have become one of the most serious diseases threatening human health and living quality.[1] As one of the most powerful and irreplaceable therapeutic methodologies, radiotherapy (RT) is employed to treat 65−75% of microscopic tumor extensions, primary and metastatic solid tumors, and regional lymph nodes at different stages.[2−5] By taking advantage of high-intensity ionizing radiation including electrons, protons, or photons (X-rays, γ-rays), RT can induce oxidative stress and/or DNA double-strand damage upon the generation of considerable cytotoxic reactive oxygen species (ROS), leading to apoptosis and death of irradiated tumor cells.[6−9] However, the complete eradication of tumor cells based on RT is still challenging to realize because of its toxic effects on adjacent normal tissues and the emergence of radiation resistance.[10,11] Utilizing radiosensitizers to absorb and deposit ionizing irradiation energy to maximize the radiation-induced tumor damage but weaken their potential side effects may open a way to overcome these limitations.[12−14] Until now, many radiosensitizers containing high-Z elements have been explored to improve the radiotherapeutic efficacy.[15−17] Among these radiosensitizers, bismuth (Bi)-based nanomaterials attract particular interests because of their high atomic number element ($Z = 83$), K-edge value (90.5 keV) and excellent X-ray attenuation properties (5.74 $cm^2\ g^{-1}$ at 100 keV).[18−22] More importantly, despite it being a heavy metal, Bi is considered a chemically stable, environmentally friendly, and nontoxic element with wide applications in the field of pharmaceuticals and cosmetics.[23,24] Thus, exploring biocompatible and efficient Bi-based nanomaterials as radiosensitizers is of great significance in improving the therapeutic efficacy of RT.

In addition to H_2O radiolysis, ionizing radiation can be used to excite photosensitizers to generate ROS for dynamic therapy. This concept has already given birth to a new treatment strategy named radiodynamic therapy (RDT).[25−29] Unlike photodynamic therapy (PDT), which was strongly

Received: May 16, 2020
Accepted: July 10, 2020
Published: July 10, 2020

restricted by the shallow infiltration of ultraviolet, visible, or even near-infrared light into biological tissue, ionizing radiation can be precisely delivered to orthotopic tumors located inside tissues or organs with no depth restriction.[30,31] As a result, considerable progress has been achieved in the development of RDT.[25−27,32] So far, most RDT relies on the use of nanoscintillators as energy transducers to activate photosensitizers via radiative or non-radiative transfer.[32−34] However, the low transfer efficiency between nanoscintillators and photosensitizers associated with their relative spatial distributions and concentrations still need further optimization. Because of the particular band structure of the valence band (VB) and conduction band (CB), it was recently reported that ionizing irradiation-induced low-energy electrons can directly excite semiconductor nanomaterials to produce electron−hole pairs for the generation of ROS.[35] Upon constructing heterojunction nanostructures with suitable band alignment, an extra internal electric field can further be established to promote electron−hole pair separation and then enhance the RDT therapeutic efficacy of semiconductor nanomaterials.[36] In addition, it is known that the tumor microenvironment featured by hypoxia can not only cause irreversible tumor angiogenesis and metastasis but also result in hypoxia-associated resistance to the therapeutic approaches that rely on the presence of molecular oxygen.[18,36−38] Photothermal therapy (PTT), which employs photothermal agent to generate regional hyperthermia via NIR light excitation to ablate tumor cells, can remarkably boost intratumoral blood flow and subsequently alleviate hypoxia status in tumor tissues, making tumor cells more sensitive to RT and RDT.[18,36−41] Therefore, it is reasonable to believe that using RT/RDT as the primary treatment along with PTT as the supplementary treatment will bring a superior synergistic effect for tumor therapy without metastasis and recurrence.

Multimode imaging is preferred to accurately identify the size and location of tumors, real-time monitor, and evaluate the therapeutic efficacy to realize effective, safe, and personalized tumor therapy, as each single imaging modality has its intrinsic restrictions.[42,43] Different from assorted imaging techniques, X-ray computed tomography (CT) imaging can provide 3D visualization with precise anatomical details on the basis of its enhanced hard-tissue contrast.[43] As a compensation, photoacoustic (PA) imaging induced by NIR absorption and subsequent thermal expansion is harnessed to render much higher spatial resolution to soft tissues and offer real-time monitoring.[44,45] Upon integrating the advantages of CT and PA, more precise imaging and diagnosis data can be obtained.[46] Herein, we demonstrate on the design and preparation of Tween-20-modified $BiVO_4@Bi_2S_3$ heterojunction nanorods (HNRs) for multimodal CT/PA imaging and RT/RDT/PTT synergistic therapy. Compared with nanospheres, nanorods have reduced steric hindrance and viscous drag near the vessel pore walls during blood transport as well as an enhanced ability to penetrate the tumor cell membranes, which greatly accelerate the accumulation of $BiVO_4@Bi_2S_3$ HNRs in tumor tissues and cells.[47,48] Benefiting from the high X-ray attenuation coefficient of Bi, $BiVO_4@Bi_2S_3$ HNRs possess a sensitive CT imaging capacity and radiation enhancement effect during RT. Meanwhile, the strong NIR absorption of Bi_2S_3 endows $BiVO_4@Bi_2S_3$ HNRs with an excellent PA imaging and photothermal transformation capacity. More importantly, the type II band alignment between $BiVO_4$ and Bi_2S_3 can greatly promote the generation and separation of electron−hole pairs, leading to enhanced RDT therapeutic efficacy. At last, in vitro and in vivo experiments are systematically performed to study the imaging and therapy properties of $BiVO_4@Bi_2S_3$ HNRs, and the results provide solid evidence to verify that our $BiVO_4@Bi_2S_3$ HNRs can be used as the nanotheranostic platform for multimodal imaging and synergistic therapy of tumors with ideal therapeutic efficacy.

2. EXPERIMENTAL SECTION

2.1. Materials. Tween-20, thioacetamide (TA, > 99%), NH_4VO_3 (99.9%), and $Bi(NO_3)_3{\cdot}5H_2O$ (99.0%) were purchased from Aladdin. Oleylamine (OLA, > 70%), octadecene (ODE, 90%), and oleic acid (OA, 90%) were purchased from Sigma-Aldrich. Cell counting kit-8 (CCK-8), crystal violet staining solution, ROS assay kit, $\bullet O^{2-}$ assay kit, immunol staining blocking buffer, and Hoechst 33342 were purchased from Beyotime. γ-H2AX (phospho S139) antibody [EP854(2)Y] (Alexa Fluor 568) (ab206901) was purchased from Abcam.

2.2. Synthesis of $BiVO_4@Bi_2S_3$ HNRs. The synthesis of $BiVO_4@Bi_2S_3$ HNRs is described below. First, 1 mmol of $Bi(NO_3)_3{\cdot}5H_2O$, 10 mL of ODE, 2 mL of OA, and 2 mL of OLA were added into a three-necked flask, followed by heating at 175 °C under a nitrogen atmosphere. When $Bi(NO_3)_3{\cdot}5H_2O$ was dissolved completely, the solution was cooled to 130 °C, followed by the addition of 0.8 mmol of NH_4VO_3 dissolved in boiling water (10 mL). The solution was maintained at 100 °C for another 30 min under vigorous stirring, followed by the addition of TA aqueous solution (1 M) with the dropping rate of 25 μL/min. After that, the solution was cooled. Ten milliliters of ethanol was added and mixed with reaction solution uniformly. When the solution was stratified, the aqueous solution (lower layer) was discarded, whereas the organic solution (upper layer) was added to10 mL of water and 10 mL of ethanol again. This process was repeated four times. Subsequently, ethanol was added to the organic solution, and the mixture was centrifuged at 6000 rpm for 3 min. The precipitate was collected and dissolved in 10 mL of *n*-hexane. This process was repeated three times. Finally, the precipitate was dissolved in cyclohexane. The synthesis of $BiVO_4$ nanorods (NRs) was similar to $BiVO_4@Bi_2S_3$ HNRs but without the addition of TA.

2.3. Surface Modification by Tween-20. The surface modification of Tween-20 is carried out using the literature methods.[19] Forty milligrams of $BiVO_4@Bi_2S_3$ HNRs was dissolved in 16 mL of cyclohexane, followed by adding 200 μL of Tween-20. The mixture was sonicated for 10 min, and then deionized water was added. After that, the mixture was kept at 70 °C for 2 h under stirring. Finally, the resulting solution was centrifuged at 13 000 rpm for 15 min. The precipitate was collected and dissolved in deionized water. The final $BiVO_4@Bi_2S_3$ HNRs were stored in deionized water at room temperature.

2.4. ROS Analysis. The spectroscopy method was used to detect and identify ROS generated by $BiVO_4@Bi_2S_3$ HNRs under X-ray irradiation. All NRs and HNRs need to be removed by centrifugation before testing the absorption or fluorescence spectrum. The yield of ROS was estimated upon measuring the fluorescence spectroscopy of solution containing HNRs and 2,7-dichlorodihydrofluorescein (DCFH). Twelve and a half microliter of 2,7-dichlorodihydrofluorescein diacetate (DCFH-DA), 0.5 mL of DMSO, and 2 mL of NaOH solution (0.01 M) are mixed and stirred for 0.5 h. Subsequently, 10 mL of phosphate buffer solution (0.25 mM, pH 7.2) is added to obtain the DCFH solution (excitation wavelength: 488 nm). The concentration of HNRs is 100 μg/mL. The yield of •OH was estimated upon measuring the fluorescence spectra change of solution containing HNRs and disodium terephthalate (excitation wavelength: 310 nm). The concentration of disodium terephthalate and HNRs were 0.02 mM and 100 μg/mL respectively. The yield of $\bullet O^{2-}$ was estimated upon measuring the absorbance change of solution containing HNRs and WST-1 ($\bullet O^{2-}$ assay kit) at 450 nm. The concentration of HNRs was 100 μg/mL. The yield of $^1O_2$ was

https://dx.doi.org/10.1021/acsabm.0c00573
ACS Appl. Bio Mater. XXXX, XXX, XXX−XXX

estimated upon measuring the absorbance change of solution containing HNRs and 9,10-diphenylanthracene at 355 nm. The concentrations of 9,10-diphenylanthracene and HNRs were 0.05 mM and 100 μg/mL, respectively. The X-ray source of the above experiment used PXi X-RAD 320 X-ray irradiator (180 kV, 6 Gy).

2.5. Cytotoxicity Assay. CCK-8, human mesenteric artery vascular endothelial (Ealy926) cells, and oral epithelial carcinoma (KB) cells were used to test the cytotoxicity of $BiVO_4$@Bi_2S_3 HNRs. Cells were cultured in a 96-well plate (8000 cells per well) and incubated at 37 °C with 5% CO_2 for 24 h, then cocultivated with different concentrations of HNRs for another 24 h. After that, the medium was removed and the cells were washed by phosphate buffer saline (PBS) for 2 times. Solarbio 1640 medium was readded with 10 μL of CCK-8, and the cells were incubated for another 2 h. At last, the microplate reader was employed to measure the absorbance at 450 nm.

2.6. Clonogenic Assay. KB cells were cultured in a 6-well plate (2000 cells per well). After cocultivation with $BiVO_4$@Bi_2S_3 HNRs (100 μg/mL) overnight, cells were treated by X-ray (0, 2, 4, 6, 8 Gy) and NIR (0.33 W/cm^2, 10 min) then washed by PBS three times. After that, the medium is readded and the cells were incubated for another 10 days. At last, the cells were stained by crystal violet staining solution. The mean surviving fraction was obtained from three parallel samples. The surviving fraction was estimated by (surviving colonies)/(cells seeded × plating efficiency).[36] And the survival curves can be fitted to the equation: surviving fraction = $\exp[-(\alpha D+\beta D^2)]$.[36] The sensitizer enhancement ratio (SER) was calculated as the ratio of the surviving fraction curve.[36] SER in the HNRs+X-ray and HNRs+X-ray+NIR groups were 1.49 and 2.11, respectively.

2.7. Apoptosis Assay. KB cells were cultured in a 6-well plate (50 000 cells per well). After complete adherence, the cells were cultured with $BiVO_4$@Bi_2S_3 HNRs (20 μg/mL) overnight. The cells were then treated by X-ray (4 Gy) or NIR (0.33 W/cm^2, 5 min) and further cultured for 24 h. Annexin V-fluorescein isothiocyanate isomer/propidium iodide (Annexin V-FITC/PI) double staining was used for apoptosis analysis using flow cytometry.

2.8. ROS in Cells. ROS assay kit was used to detect ROS in cells. KB cells were cultured in a 6-well plate (80 000 cells per well). After cocultivation with $BiVO_4$@Bi_2S_3 HNRs (100 μg/mL) overnight, cells were washed by PBS three times. DCFH-DA (10 μM) was then added to each well, followed by incubation for 20 min and washing by PBS three times. After that, the cells were treated by X-ray (6 Gy) or NIR (0.33 W/cm^2, 10 min) and observed using the FV1000 laser scanning confocal microscopy (emission wavelength, 525 nm; excitation wavelength, 488 nm).

2.9. DNA Double-Stranded Breaks. KB cells were cultured in a 6-well plate (80 000 cells per well). After cocultivation with $BiVO_4$@Bi_2S_3 HNRs (100 μg/mL) overnight, cells were treated by X-ray (6 Gy) or NIR (0.33 W/cm^2, 10 min). After continuing to cultivate for 2 h, cells were fixed by paraformaldehyde (4%) for 10 min, followed by washing by PBS three times. Cells were then permeabilized with methanol for 15 min and washed by PBS three times. After that, cells were exposed in immunol staining blocking buffer for 2 h and further incubated with 100-fold γ-H2AX (phospho S139) antibody [EP854(2)Y] (Alexa Fluor 568) (ab206901) (emission wavelength, 603 nm; excitation wavelength, 578 nm) at 4 °C overnight and washed by PBS three times. Sequentially, cells were stained with Hoechst 33342 (emission wavelength, 461 nm; excitation wavelength, 350 nm) and washed by PBS three times. At last, the cells were observed by using FV1000 laser scanning confocal microscopy.

2.10. In Vivo RT/PTT Synergistic Treatment. The right legs of BALB/c female nude mice were subcutaneously implanted with 1.5 × 10^6 KB cells suspended in 100 μL of 1640 medium. As the average tumor volume reached 75 mm^2, the mice were randomly divided into seven groups according to different treatments: (i) PBS, (ii) HNRs, (iii) NIR, (iv) X-ray, (v) HNRs+NIR, (vi) HNRs+X-ray, and (vii) HNRs+NIR+X-ray. The tumor-bearing nude mice in groups (ii), (v), (vi), and (vii) were injected with 20 μL of HNRs (5 mg/mL) intratumorally. Mice in the corresponding groups were then treated by NIR (0.33 W/cm^2, 20 min) or X-ray (6 Gy) irradiation. Tumor volumes and body weights of each group of mice were recorded after treatments. The tumor volume is calculated as $D^2L/2$ (D/L represents the short/long axis length of tumors, respectively). At last, all the mice were sacrificed and the blood, hearts, livers, spleens, lungs, kidneys, and tumors were taken. The blood was centrifuged and the serum was taken for blood analysis. The organs and tumors were weighed and used for H&E staining.

2.11. CT Imaging. U-SPECT+/CT (MILABS) was used for in vitro and in vivo CT imaging. Different concentrations of HNRs and iobitridol aqueous solutions were prepared for in vitro imaging. Tumor-bearing BALB/c nude mice were intratumorally injected with 50 μL of HNRs (10 mg/mL) for in vivo imaging.

2.12. PA Imaging. MSOT INVISIO-256 (iThera Medical) was used for in vitro and in vivo PA imaging. Different concentrations of HNRs aqueous solutions were prepared for in vitro imaging. Tumor-bearing BALB/c nude mice were intratumorally injected with 20 μL of HNRs (10 mg/mL) for in vivo imaging.

2.13. Characterization. X-ray diffraction (XRD) was measured by an Empyrean X-ray diffractometer with Cu K radiation (λ = 1.5418 Å). Transmission electron microscope (TEM) and energy-dispersive X-ray spectroscopy (EDS) were carried out on a JEM-2100F electron microscope (200 kV) coupled with an EDS detector. UV−vis spectra were taken by a Shimadzu UV-3600 UV−vis spectrometer. X-ray photoelectron spectroscopy (XPS) and ultroviolet photoelectron spectrometer (UPS) was carried out on a PREVAC sp.z.0.0 R3000 spectrometer with an Al KR excitation (1486.7 eV). Fourier transform infrared spectroscopy (FTIR) was measured by a Bruker VERTEX 80 V. The zeta potential was measured by a Zetasizer NanoZS (Malvern). Electron paramagnetic resonance (EPR) spectra were recorded on an E500 CW-EPR spectrometer (Bruker ELEXSYSII). The Bi^{3+} concentration was measured by inductive coupled plasma emission spectrometer (ICP) measurements with the PerkinElmer Optima 3300DV.

2.14. Statistical Analysis. Statistical analyses were performed using Statistical Product and Service Solutions (SPSS) software for Windows. The experimental results are presented as means ± standard deviation. Groups were compared using one-way analysis of variance. $P < 0.05$ was considered to be statistically significant.

3. RESULTS AND DISCUSSION

The synthesis and applications of Tween-20-modified $BiVO_4$@Bi_2S_3 HNRs for multimodal CT/PA imaging and RT/RDT/PTT synergistic therapy are illustrated in Scheme 1. In a typical synthesis, $BiVO_4$ NRs are first prepared by dissolving $Bi(NO_3)_3{\cdot}5H_2O$, OA, and OLA in ODE at 175 °C, followed by refluxing under vigorous stirring for 30 min after the injection of NH_4VO_3. Then, aqueous solution of TA is

Scheme 1. Schematic Representation for the Synthesis and Applications of Tween-20-Modified $BiVO_4$@Bi_2S_3 HNRs for Multimodal CT/PA Imaging and RT/RDT/PTT Synergistic Therapy

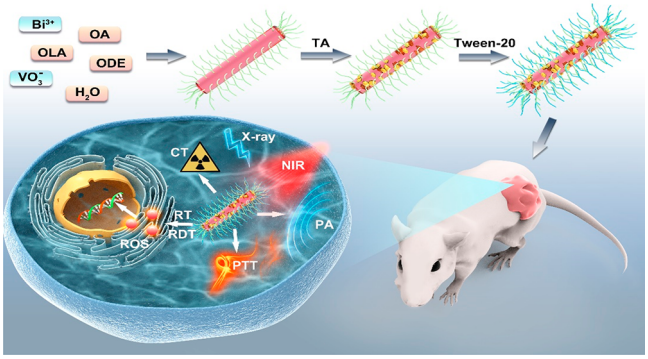

https://dx.doi.org/10.1021/acsabm.0c00573
ACS Appl. Bio Mater. XXXX, XXX, XXX−XXX

dropwise added into the reaction solution to trigger the anion-exchange between VO_4^{3-} and S^{2-}. After that, the as-prepared $BiVO_4@Bi_2S_3$ HNRs are isolated through centrifugation, followed by washing with hexane and ethanol for three times. Because it has been reported that the unique molecular structure of Tween-20 can enable NRs with good dispersibility but protect NRs from nonspecific adsorption of proteins, facilitating the accumulation of NRs in tumor tissues and cells upon the enhanced permeation and retention effect, Tween-20 is employed to cover the surface of $BiVO_4@Bi_2S_3$ HNRs through hydrophobic−hydrophobic interaction to improve their biocompatibility and dispersibility in physiological solution but minimize the cytotoxicity.[18,19,49] It is noted that the composition of the $BiVO_4@Bi_2S_3$ HNRs is tunable by changing the dosage of TA during anion-exchange. By increasing TA from 1.0 to 2.5 mmol, the proportion of Bi_2S_3 in $BiVO_4@Bi_2S_3$ HNRs increases apparently. Accordingly, the products are designated as $BiVO_4@Bi_2S_3$-1 (1.0 mmol TA), $BiVO_4@Bi_2S_3$-2 (1.5 mmol TA), $BiVO_4@Bi_2S_3$-3 (2.0 mmol TA), and $BiVO_4@Bi_2S_3$-4 (2.5 mmol TA), respectively.

Figure 1 shows TEM images of $BiVO_4@Bi_2S_3$-4 HNRs, from which it can be seen that the as-prepared $BiVO_4$ are uniform

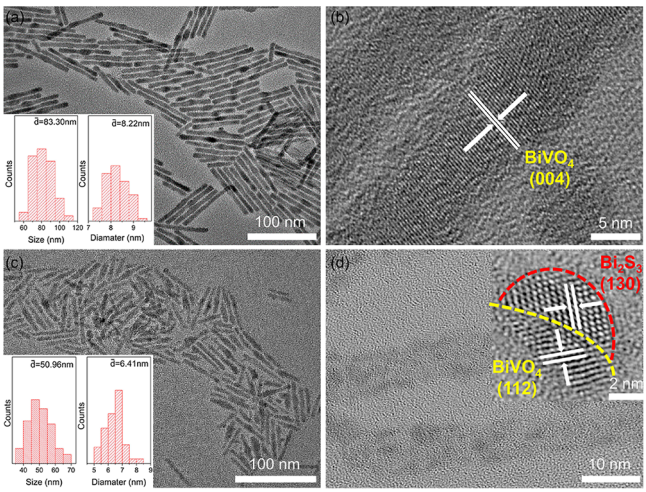

Figure 1. (a) TEM and (b) HRTEM images of $BiVO_4$ NRs. (c, d) TEM images of $BiVO_4@Bi_2S_3$-4 HNRs under different magnifications. Insets in a and c show size distributions of $BiVO_4$ NRs and $BiVO_4@Bi_2S_3$-4 HNRs. Inset in d shows HRTEM images of $BiVO_4@Bi_2S_3$-4 HNRs.

NRs with an average length and width of 83.30 and 8.22 nm. High-resolution TEM (HRTEM) exhibits a well-formed monocrystal with interplanar spacing of 0.30 nm, consistent with the (004) crystal plane of monoclinic $BiVO_4$. After anion-exchange, the $BiVO_4@Bi_2S_3$ HNRs still retain a rodlike morphology (Figure 1c). However, both the length and width of HNRs are shrunk compared with the initial $BiVO_4$ NRs. In the meantime, many dark and irregular domains appear on the surface of HNRs (Figure 1d). With the help of HRTEM, two sets of lattice fringes with the clear boundary can be observed. The interplanar spacing of the darker area is 0.35 nm, which corresponds to the (130) crystal plane of orthogonal Bi_2S_3. In contrast, the interplanar spacing of the lighter area is 0.32 nm, consistent with the (112) crystal plane of monoclinic $BiVO_4$. The results from the HRTEM image reveal that the darker areas on the surface of HNRs should be Bi_2S_3, whereas the lighter areas of the HNRs are supposed to be $BiVO_4$. The element distribution of $BiVO_4@Bi_2S_3$-4 HNRs characterized by EDS elemental mapping further suggests the presence of Bi_2S_3 on the surface of $BiVO_4$ (Figure S1). TEM images of $BiVO_4@Bi_2S_3$-1, $BiVO_4@Bi_2S_3$-2, and $BiVO_4@Bi_2S_3$-3 HNRs are also exhibited in Figure S2. Because thiols have the chemical etching ability to drag metal atoms away from the surface of the nanoparticles, whereas a large excess of TA is used in our synthesis process, TA plays not only as the sulfur source but also as the etchant during the anion-exchange.[50,51] As a result, the size of $BiVO_4@Bi_2S_3$ HNRs is smaller than that of $BiVO_4$ NRs. The aqueous dispersibility of $BiVO_4@Bi_2S_3$ HNRs after surface modification by Tween-20 is excellent. FTIR is first used to identify the successful surface modification of Tween-20 on $BiVO_4@Bi_2S_3$ HNRs (Figure S3). The TEM image shown in Figure S4a then presents the well monodispersed Tween-20 capped $BiVO_4@Bi_2S_3$ HNRs. The corresponding solutions are totally clear and transparent, and can be stored for a month without obvious aggregation or sediment (Figures S4b and S5).

Figure 2a exhibits the XRD patterns of $BiVO_4@Bi_2S_3$ HNRs. The as-prepared $BiVO_4$ NRs are monoclinic scheelite structures (JCPDS 83-1699). Upon the addition of TA, the intensities of diffraction peaks belonging to $BiVO_4$ (at 19 and 31°) gradually decrease. Instead, the characteristic peaks associated with orthorhombic Bi_2S_3 (JCPDS 17-0320) at 22 and 25° start to appear in a pattern of $BiVO_4@Bi_2S_3$-1 and can be clearly observed in patterns of $BiVO_4@Bi_2S_3$-3 and $BiVO_4@Bi_2S_3$-4. UV−vis absorption spectra of $BiVO_4@Bi_2S_3$ HNRs are shown in Figure 2b, which not only extend to the NIR region due to the presence of Bi_2S_3, but also enhance remarkably as the proportion of Bi_2S_3 increases. The compositions of $BiVO_4@Bi_2S_3$ HNRs are characterized by EDS. As manifested in Figure 2c and Table 1, the atomic ratio between Bi and V in $BiVO_4$ NRs is 1:0.64, which deviates from the stoichiometric ratio of 1:1 due to their anisotropic structures.[52] Along with the exchange between S^{2-} and VO_4^{3-}, the proportion of V decreases accompanied by the increase of S. The enlarged spectrum of Figure 2c in the range from 2 to 3 eV clearly indicates the enhancement of S (Figure 2d). And the atomic ratio between S and V in $BiVO_4@Bi_2S_3$-4 HNRs can be as high as 0.87:0.24 (Table 1).

XPS is further used to investigate the valence states of elements in $BiVO_4@Bi_2S_3$ HNRs (Figures S6 and S7). The Bi spectrum of $BiVO_4$ NRs has two peaks at 164.3 and 159.1 eV, assigned to $4f_{5/2}$ and $4f_{7/2}$ of Bi^{3+}.[52] As for $BiVO_4@Bi_2S_3$ HNRs, a 0.3 eV shift to high energy can be found that is due to the appearance of a new pair of peaks at 164.8 and 159.5 eV, which can be attributed to Bi^{3+} in Bi_2S_3.[18] In addition, both $BiVO_4@Bi_2S_3$ HNRs and $BiVO_4$ NRs exhibit characteristic peaks at 524.5 and 516.8 eV, corresponding to the existence of V^{5+}.[53] In addition, the O 1s spectra of $BiVO_4@Bi_2S_3$ HNRs and $BiVO_4$ NRs can be divided into three peaks. After annealing at 400 °C for 30 min, the peaks at 529.0 and 531.2 eV remain unchanged, but the peak at 531.8 eV greatly weakens and even disappears. Thus, it is speculated that the peak at 529.0 eV belongs to O^{2-} in Bi−O bond, whereas peaks at 531.2 and 531.8 eV are related to the surface-adsorbed O_2 and the ligands, respectively (Figures S6d, S7d, and S8).[53,54] Unlike $BiVO_4$ NRs, there is an extra broad peak located around 162 eV in the spectrum of $BiVO_4@Bi_2S_3$ HNRs that corresponds to the S^{2-} of Bi_2S_3.[18]

Because the presence of Bi_2S_3 brings $BiVO_4@Bi_2S_3$ HNRs strong absorption in NIR region, the photothermal conversion

https://dx.doi.org/10.1021/acsabm.0c00573
ACS Appl. Bio Mater. XXXX, XXX, XXX−XXX

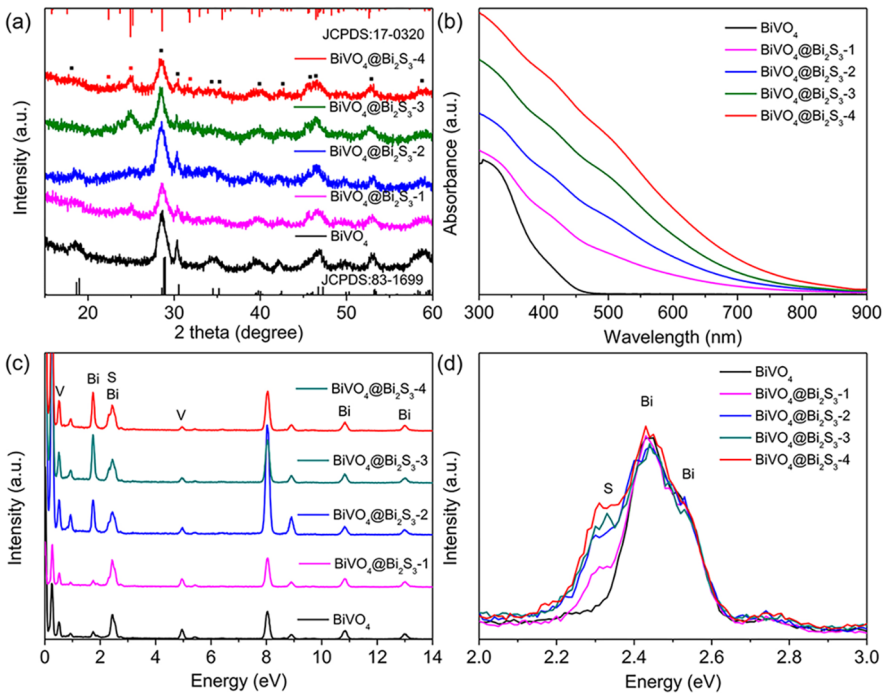

Figure 2. (a) XRD patterns and (b) UV−vis absorption spectra of $BiVO_4@Bi_2S_3$ HNRs and $BiVO_4$ NRs. (c, d) EDS spectra of $BiVO_4@Bi_2S_3$ HNRs and $BiVO_4$ NRs.

Table 1. Elemental Composition of $BiVO_4@Bi_2S_3$ HNRs and $BiVO_4$ NRs Obtained by EDS

element	Bi	V	S
NRs	1	0.64	0
HNRs-1	1	0.55	0.44
HNRs-2	1	0.43	0.62
HNRs-3	1	0.32	0.77
HNRs-4	1	0.24	0.87

capability of $BiVO_4@Bi_2S_3$ HNRs in aqueous solution are evaluated upon 808 nm irradiation. As illustrated in Figure 3a−c, the temperature of $BiVO_4@Bi_2S_3$ HNR aqueous solution rises rapidly by increasing the irradiation duration or the proportion of Bi_2S_3. At the same time, the photothermal conversion capability of $BiVO_4@Bi_2S_3$ HNRs is highly determined by the applied laser power density and the HNR concentration. Upon 10 min irradiation with a power density of 2 W/cm^2, the temperature of the aqueous solution containing 500 μg/mL $BiVO_4@Bi_2S_3$-4 HNRs exhibits a remarkable increase of 40 °C. In sharp comparison, only a tiny temperature change of 1 °C in pure water can be observed under the same conditions. According to the previously reported model, the photothermal conversion efficiency of $BiVO_4@Bi_2S_3$-4 HNRs is calculated to be 22.4%, which is equivalent to that of other Bi-containing materials (Figure S9).[37] The photothermal stability of $BiVO_4@Bi_2S_3$ HNRs is also exhibited in Figure 3d. The $BiVO_4@Bi_2S_3$ HNRs dispersion can keep the 40 °C increment after four cycles of heating/cooling processes, suggesting their excellent photothermal stability. The promising photothermal conversion capability and ideal photothermal stability endow $BiVO_4@Bi_2S_3$ HNRs great potential for PA imaging and PTT of tumors.

The radiosensitivity of $BiVO_4@Bi_2S_3$ HNRs is then assessed. The fluorescence spectra of DCFH, which is in proportion to the yield of ROS, are first used to estimate the ability of $BiVO_4@Bi_2S_3$ HNRs to generate ROS under X-ray irradiation.[55] As shown in Figure 4a, the ROS yield increases apparently with an increasing proportion of Bi_2S_3 in $BiVO_4@Bi_2S_3$ HNRs. $BiVO_4@Bi_2S_3$-4 HNRs exhibit 1.6 times higher generation of ROS under X-ray irradiation than $BiVO_4$ NRs. Subsequently, the species of ROS generated by $BiVO_4@Bi_2S_3$ HNRs are identified by using disodium terephthalate, WST-1, and 9,10-diphenylanthracene as •OH, $•O_2^-$, and $^1O_2$ indicators.[37,56,57] As shown in Figure 4b−d, the presence of $BiVO_4@Bi_2S_3$ HNRs or $BiVO_4$ NRs has no effect on the fluorescence intensity of disodium terephthalate aqueous solution, suggesting they are powerless to generate •OH under X-ray irradiation. However, the absorbance of WST-1 increases obviously in the presence of $BiVO_4@Bi_2S_3$ HNRs, whereas only a tiny increase can be observed in WST-1 aqueous solution containing $BiVO_4$ NRs. This result indicates that $BiVO_4@Bi_2S_3$ HNRs can generate a large amount of $•O_2^-$, which is about 4.36 times higher than that of $BiVO_4$ NRs. By comparing the absorbance of 9,10-diphenylanthracene, it is known that the amount of $^1O_2$ generated by $BiVO_4@Bi_2S_3$ HNRs is only slightly lower than that of $BiVO_4$ NRs, but obviously higher than that of deionized water.

The mechanism of $BiVO_4@Bi_2S_3$ HNRs on generating ROS is investigated. The energy level diagram of $BiVO_4@Bi_2S_3$ HNRs are constructed on the basis of the analysis by UPS and UV−vis absorption spectrum (Scheme 2). The VB and CB of $BiVO_4$ and Bi_2S_3 are identified as 2.51, 0.04, 1.20, and −0.12 eV, respectively (Figure S10). Under irradiation, the excited electrons in CB of Bi_2S_3 will migrate to CB of $BiVO_4$.[58] In contrast, holes in the VB of $BiVO_4$ prefer migrating to the VB of Bi_2S_3.[58] Thus, the heterojunction structure between $BiVO_4$ and Bi_2S_3 can efficiently inhibit the recombination between electrons and holes. Photocurrent and impedance tests further provide evidence to demonstrate that the heterojunction structure of $BiVO_4@Bi_2S_3$ HNRs can promote charge

https://dx.doi.org/10.1021/acsabm.0c00573
ACS Appl. Bio Mater. XXXX, XXX, XXX−XXX

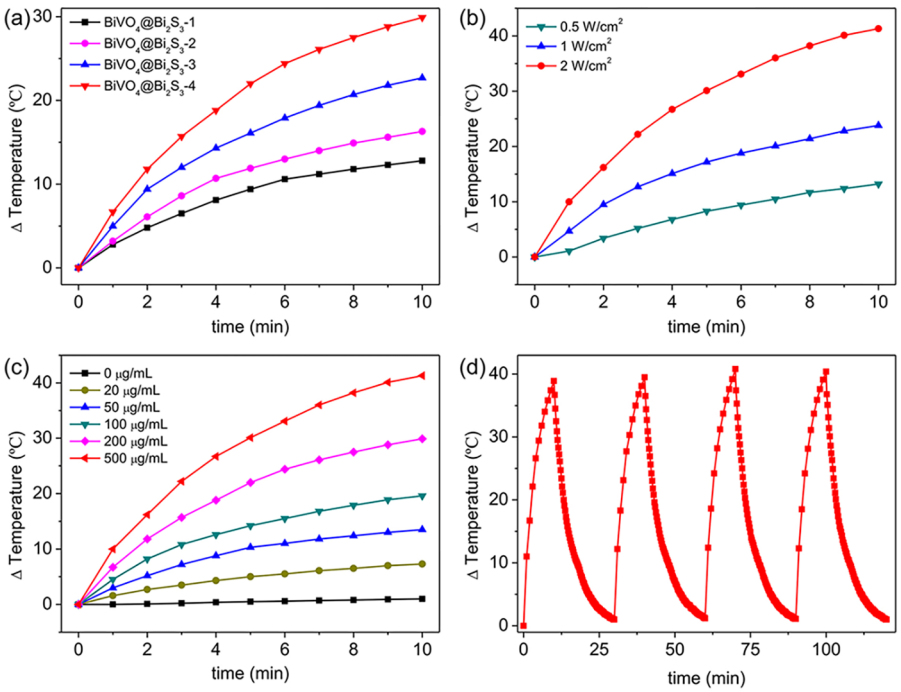

Figure 3. (a) Temperature increment vs the proportion of Bi_2S_3 in HNRs (500 μg/mL HNRs; 2 W/cm^2 irradiation), (b) the power density of incident laser (500 μg/mL $BiVO_4$@Bi_2S_3-4 HNRs), (c) the concentration of HNRs ($BiVO_4$@Bi_2S_3-4 HNRs; 2 W/cm^2 irradiation). (d) Photothermal stability of HNRs (500 μg/mL $BiVO_4$@Bi_2S_3-4 HNRs; 2 W/cm^2 irradiation).

separation under irradiation. Compared with $BiVO_4$ NRs, $BiVO_4$@Bi_2S_3 HNRs exhibit higher current density, lower resistance, and faster responsiveness (Figure 4e, f). Because •OH is mainly formed by the oxidation of H_2O. Although X-ray-induced electrons and holes can be efficiently separated in $BiVO_4$@Bi_2S_3 HNRs, holes in the VB of Bi_2S_3 do not have enough energy to oxidize H_2O to form •OH.[56] As for $BiVO_4$ NRs, despite the VB of $BiVO_4$ NRs being more positive than the redox potential of •OH/H_2O, the rapid recombination of electrons and holes seriously shrinks their efficient for •OH generation. As a result, neither $BiVO_4$@Bi_2S_3 HNRs or $BiVO_4$ NRs can generate •OH under X-ray irradiation.

Different from •OH, •O_2^- mainly derives from the reduction of O_2. Although a large number of •O_2^- are produced by $BiVO_4$@Bi_2S_3 HNRs under X-ray irradiation, the electrons in CB of neither $BiVO_4$ nor Bi_2S_3 are thermodynamically accessible for driving the redox reaction from O_2 to •O_2^-.[56] Recently, it is reported that the oxygen vacancies (V_O) on the surface of photocatalysts can serve as the electron trap centers to inhibit the charge recombination. As a result, V_O with abundant localized electrons can remarkably promote the adsorption and coordination of O_2, followed by the charge transfer from V_O to the adsorbed O_2 to activate the formation and release of •O_2^-.[59−61] Figure S11 exhibits the EPR spectra of $BiVO_4$@Bi_2S_3 HNRs without and with annealing. From which it can be seen that the as-prepared $BiVO_4$@Bi_2S_3 HNRs possess a strong signal at g = 2.002, whereas no signal is detectable in the EPR spectrum of HNRs experienced annealing in the open air.[59] Because annealing in the open air is a universal method to eliminate V_O, it is reasonable to believe that our $BiVO_4$@Bi_2S_3 HNRs possess a large number of V_O.

It is known that the generation of $^1O_2$ can be divided into two types: on one way, $^1O_2$ may be generated through the energy transfer from the excited photosensitizers to the triplet ground state of O_2.[62] Instead of the energy transfer, oxidizing •O_2^- via electron transfer is another way to produce $^1O_2$.[54] To identify the generation pathway of $^1O_2$, 1,4-benzoquinone (BQ) as the •O_2^- eliminator is added to the solution containing 9,10-diphenylanthracene and $BiVO_4$@Bi_2S_3 HNRs/$BiVO_4$ NRs.[63] As shown in Figure S12, the addition of BQ has no significant effect on the absorbance of 9,10-diphenylanthracene. Therefore, it is suggested that $^1O_2$ are generated by $BiVO_4$@Bi_2S_3 HNRs and $BiVO_4$ NRs via energy transfer instead of electron transfer. On the basis of the analysis above, the ROS generating process by $BiVO_4$@Bi_2S_3 HNRs under X-ray irradiation is concluded (Scheme 2). Because the heterojunction structure and the presence of V_O can effectively prolong the charge lifetime by promoting their separation, X-ray-induced electrons have a better chance to join the O_2 reduction reaction to form •O_2^-. As a result, a large number of •O_2^- and $^1O_2$ can be generated simultaneously by $BiVO_4$@Bi_2S_3 HNRs under X-ray irradiation. In contrast, X-ray-induced electrons and holes in pure $BiVO_4$ NRs are more inclined to recombine rather than separation. Because the energy of excited states can be released in various modes, only a moderate amount of $^1O_2$ with trace •O_2^- are formed by $BiVO_4$ NRs.

Because of the strongest photothermal conversion capability and ROS generation capability, $BiVO_4$@Bi_2S_3-4 HNRs, which are abbreviated as $BiVO_4$@Bi_2S_3 HNRs in the latter part of the manuscript, are chosen for subsequent in vitro and in vivo imaging and therapy. The cytotoxicity of $BiVO_4$@Bi_2S_3 HNRs is first evaluated by standard CCK-8 assay to ensure their safety for biological applications. After coculture with $BiVO_4$@Bi_2S_3 HNRs for 24 h, the cell viability of Ealy926 cells and KB cells are still above 80% even when the concentration of HNRs is as high as 200 μg/mL, suggesting no appreciable cytotoxicity of $BiVO_4$@Bi_2S_3 HNRs at the tested concentrations (Figure S13). The colloidal stability of $BiVO_4$@Bi_2S_3 HNRs in

https://dx.doi.org/10.1021/acsabm.0c00573
ACS Appl. Bio Mater. XXXX, XXX, XXX−XXX

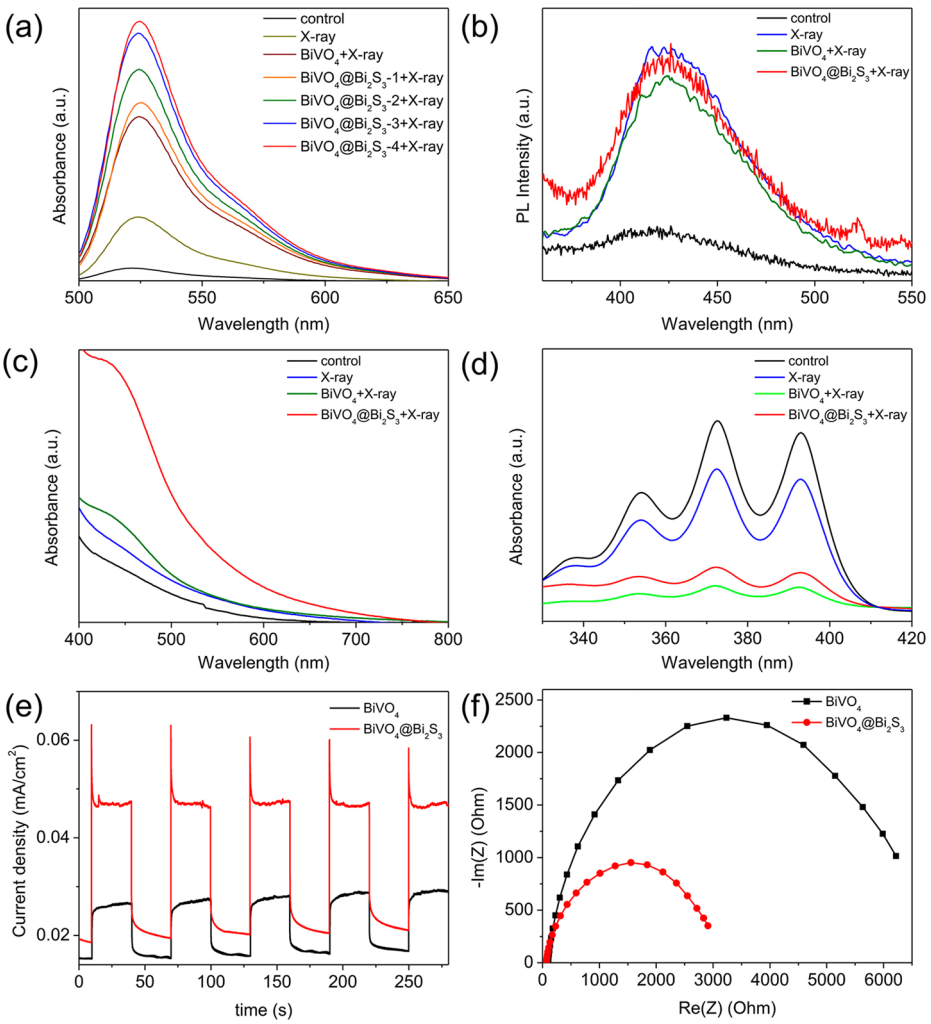

Figure 4. (a) Fluorescence spectra of ROS detection by DCFH. (b) Fluorescence spectra of •OH detection by disodium terephthalate. (c, d) UV–vis absorption spectra of $\bullet O_2^-$ and $^1O_2$ detection by WST-1 and 9,10-diphenylanthracene. (e, f) Photocurrents and impedances of $BiVO_4@Bi_2S_3$ HNRs and $BiVO_4$ NRs.

different physiological solutions are tested as well. After storage for 24 h, $BiVO_4@Bi_2S_3$ HNRs still well disperse in water, PBS, medium, and serum-containing medium (Figure S14). Lower toxicity and good colloidal stability guarantee the subsequent in vitro and in vivo experiments.

The in vitro CT imaging performance of $BiVO_4@Bi_2S_3$ HNRs is assessed by comparing with the commercially used CT contrast agent (iobitridol).[64] An ideal linear correlation between Hounsfield unit (HU) values and mass concentrations of $BiVO_4@Bi_2S_3$ HNRs is depicted (Figure 5a, b). The X-ray absorption coefficient of $BiVO_4@Bi_2S_3$ HNRs is estimated to be 30.913 HU mL mg^{-1}, which is much higher than that of iobitridol (20.360 HU mL mg^{-1}). It is noted that the proportion of the radiodense element in $BiVO_4@Bi_2S_3$ HNRs (27.89%) is much lower than that in iobitridol (91.17%), which means our $BiVO_4@Bi_2S_3$ HNRs will exhibit a better CT imaging performance than iobitridol if the molar concentrations of Bi in $BiVO_4@Bi_2S_3$ HNRs equals to I in iobitridol. In vivo CT imaging property of $BiVO_4@Bi_2S_3$ HNRs is further studied in KB tumor-bearing mice (Figure 5c). Only normal bone structures can be observed without the injection of HNRs, whereas strong CT imaging signals in the tumor site are visualized immediately after intratumoral injection of $BiVO_4@Bi_2S_3$ HNRs. Afterward, the multispectral optoacoustic tomography is employed to characterize the PA mapping of $BiVO_4@Bi_2S_3$ HNRs in vitro (Figure 5d, e). Obvious concentration-dependent PA signals are observed under NIR laser irradiation (808 nm). After intratumoral injection of $BiVO_4@Bi_2S_3$ HNRs, the PA signal intensity in the tumor site notably increases over time and reaches a peak signal at 2 h (Figure 5f). As a comparison, a negligible PA signal is visible in the tumor site without the injection of $BiVO_4@Bi_2S_3$ HNRs. These results clearly reveal that $BiVO_4@Bi_2S_3$ HNRs have the potential to act as a multimodal contrast agent for CT/PA imaging.

Thereafter, the clonogenic assay is carried out to evaluate the in vitro synergistic therapeutic efficacy of $BiVO_4@Bi_2S_3$ HNRs. The amount of HNR uptake by KB cells is first calculated by ICP. After incubation with 100 μg/mL HNRs for 24 h, the cell uptake ratio is calculated to be 11.27%. KB cells are then treated by NIR laser and X-ray in the absence and presence of $BiVO_4@Bi_2S_3$ HNRs. As shown in Figure 6, the colony formation of KB cells irradiated under NIR or X-ray can decrease to 84.2 and 48.3%, whereas only 14.1 and 10.0% cells survive under HNRs+NIR and HNRs+X-ray treatments. More importantly, KB cells treated with HNRs under both of NIR and X-ray irradiations exhibit the strongest inhibition of cancer cell proliferation with only 1.1% cell survival. In addition, by

https://dx.doi.org/10.1021/acsabm.0c00573
ACS Appl. Bio Mater. XXXX, XXX, XXX−XXX

Scheme 2. Schematic Representation for the Energy Band Structure of $BiVO_4$@Bi_2S_3 HNRs

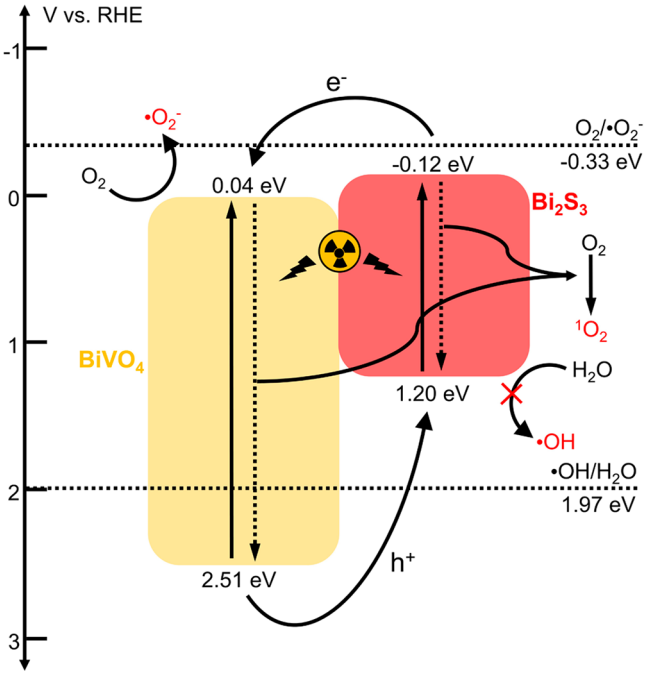

treating KB cells with HNRs plus NIR laser (1 W/cm^2) and X-ray (2, 4, 6, and 8 Gy), the same therapeutic effects can be achieved at significantly low X-ray dose (Figure 6c). Flow cytometric analysis exhibits the same tendency. As shown in Figure S15, the KB cell survival rate under the HNRs+NIR+X-ray treatment is the lowest compared with those under HNRs +NIR and HNRs+X-ray treatments. These results suggest that $BiVO_4$@Bi_2S_3 HNRs have great potential for serving as radiosensitizers and photothermal agents, and the synergistic therapeutic effect is more promising than any single treatment. Moreover, the presence of $BiVO_4$@Bi_2S_3 HNRs can withstand lower radiation doses and achieve better therapeutic effects, which is beneficial for reducing the side effects that are usually induced by excessive X-ray exposure.

DCFH-DA, which can convert to DCF with strong green fluorescent in the presence of ROS, are further used as fluorescence probes to verify the production of ROS at cellular level.[65] As depicted in Figure 6d, no fluorescence can be detected in KB cells treated by PBS, HNRs, NIR, and HNRs +NIR. Only extremely weak green fluorescence is seen in cells treated by X-ray. Cells after HNRs+X-ray treatment exhibit bright fluorescence, whereas the brightest green fluorescence signals are observed in cells under HNRs+NIR+X-ray treatment. γ-H2AX foci detection in cell nuclei by the confocal microscopy are conducted to quantitatively analyze DNA double-strand breaks as well.[66] Consisting with the cell colony assay and the DCFH-DA assay results, no chromosome damage is observed in cells without X-ray irradiation. More serious DNA damage can be found in cells treated by HNRs +X-ray than those treated by X-ray alone. And the most severe

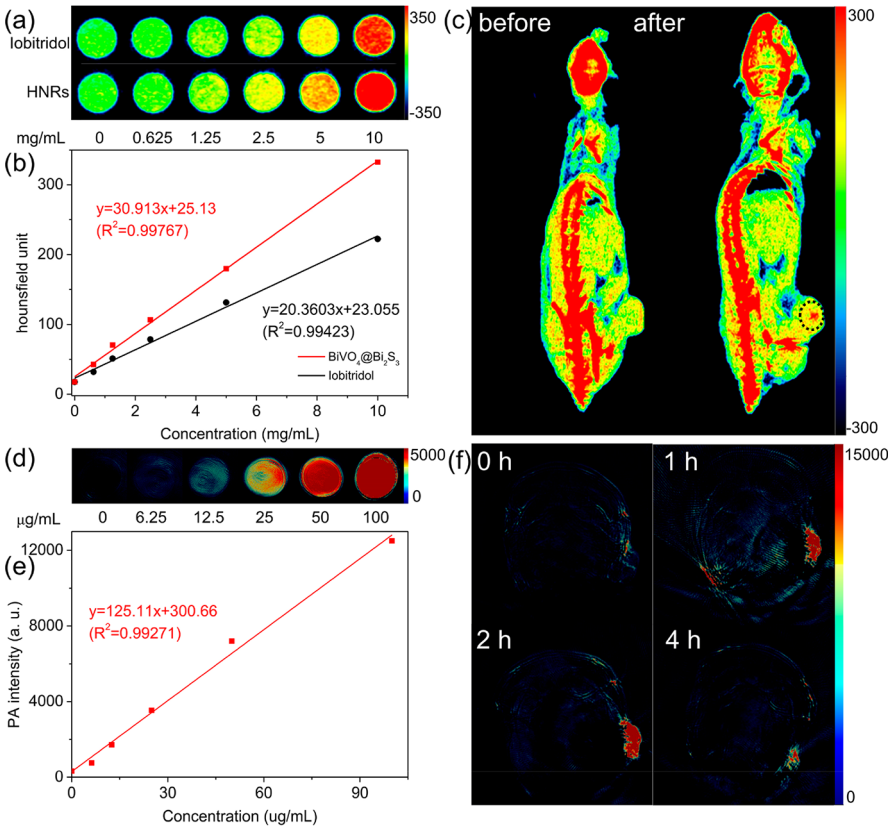

Figure 5. (a) CT images of $BiVO_4$@Bi_2S_3 HNRs and iobitridol solutions at different concentrations. (b) HU values of $BiVO_4$@Bi_2S_3 HNRs and iobitridol solutions. (c) In vivo CT images of tumors in mice obtained before and after intratumoral injection of $BiVO_4$@Bi_2S_3 HNRs. (d) PA images of $BiVO_4$@Bi_2S_3 HNRs at different concentrations. (e) PA values of $BiVO_4$@Bi_2S_3 HNRs at different concentrations. (f) In vivo PA images of tumors in mice obtained before and after intratumoral injection of $BiVO_4$@Bi_2S_3 HNRs.

https://dx.doi.org/10.1021/acsabm.0c00573
ACS Appl. Bio Mater. XXXX, XXX, XXX−XXX

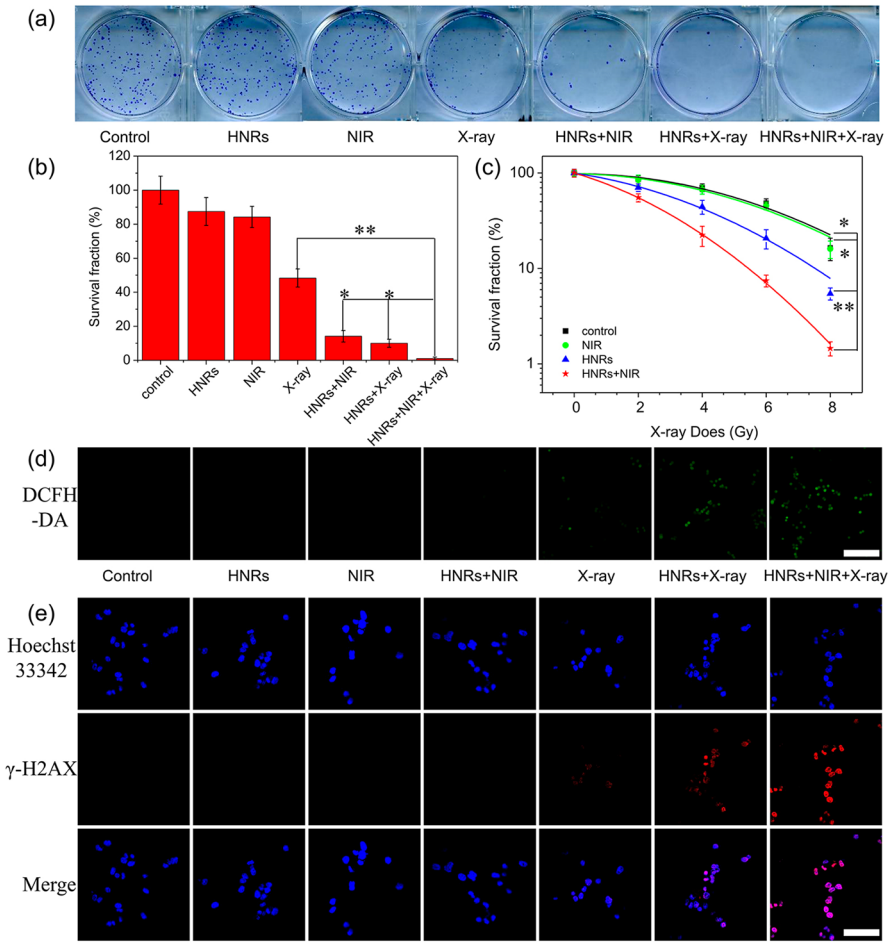

Figure 6. (a) Clonogenic assay of KB cells under different treatments (NIR: 0.33 W/cm^2 and 10 min; X-ray: 6 Gy). (b) Survival fraction of KB cells under different treatments (NIR: 0.33 W/cm^2 and 10 min; X-ray: 6 Gy). (c) Survival fraction of KB cells under different treatments and X-ray dose. (d) ROS detection in KB cells under different treatments by using DCFH-DA as the probe (scale bar is 200 μm). (e) γ-H2AX staining in KB cells under different treatments (scale bar is 40 μm). *P*-values were calculated by one-way ANOVA: $^*P < 0.05$, $^{**}P < 0.01$.

DNA damage is observed under HNRs+X-ray+NIR treatment. It is noted that in both DCFH-DA assay and γ-H2AX assay, the fluorescence intensity of the cells treated by $BiVO_4@Bi_2S_3$ HNRs is higher than that treated by $BiVO_4$ NRs (Figure S16). These results imply that $BiVO_4@Bi_2S_3$ HNRs can generate more ROS in cells than pure $BiVO_4$ NRs. Meanwhile, PTT can provide additional benefits for RT and RDT on achieving a high concentration of ROS in cells.

Encouraged by the fascinating therapeutic efficacy in vitro, in vivo antitumor efficacy of $BiVO_4@Bi_2S_3$ HNRs is evaluated. The subcutaneous KB tumor-bearing mice are divided into seven groups randomly according to various treatments: (i) PBS solution injection, (ii) HNRs injection, (iii) X-ray irradiation, (iv) NIR laser irradiation, (v) HNRs injection and X-ray irradiation, (vi) HNRs injection and NIR laser irradiation, (vii) HNRs injection and NIR laser and X-ray irradiations. Mice in group (iv), (vi), and (vii) are injected with 20 μL of PBS or $BiVO_4@Bi_2S_3$ HNRs (5 mg/mL) intratumorally, followed by irradiation under 808 nm laser with the power density of 0.33 W/cm^2. The surface temperature profiles of the tumor region are recorded by an infrared thermal camera at different time intervals (Figure 7a, b). The temperature of tumor site with HNRs injection rapidly increases by 17 °C. In marked contrast, the temperature of tumors in group (iv) is hardly changed (~5 °C) during the whole irradiation. This result manifests the well photothermal efficiency of $BiVO_4@Bi_2S_3$ HNRs, which can cause distinct localized overheat to ablate tumor but without any influence on surrounding tissues.

Sequentially, the in vivo therapeutic efficacy of $BiVO_4@Bi_2S_3$ HNRs is assessed by recording the change of tumor volumes in each group within 16 days. The results are plotted as a function of time intervals (Figure 7c). Mice in groups (i) and (ii) experience the same trend, suggesting that the single employment of HNRs fails to inhibit the growth of tumors. The tumor volumes of mice in groups (iii) and (iv) are slightly smaller than those in group (i), implying that X-ray and NIR laser irradiation can only mildly inhibit the tumor growth. In contrast, the growth of tumors in group (v) and (vi) are significantly inhibited, but there will be a recurrence at about 10 days after the treatment. Nearly complete inhibition on tumor growth is achieved in group (vii) without relapse during the experimental time period. The similar results are also displayed by the photographs and weights of tumors, which firmly verifies that the synergistic RT/RDT/PTT of HNRs possesses better antitumor performance in vivo than any single treatment. Furthermore, the weights of mice in each group are similar with slight fluctuation within the culture time, indicating the negligible side effects of all the treatments during the therapeutic process. Additionally, hematoxylin and

https://dx.doi.org/10.1021/acsabm.0c00573
ACS Appl. Bio Mater. XXXX, XXX, XXX−XXX

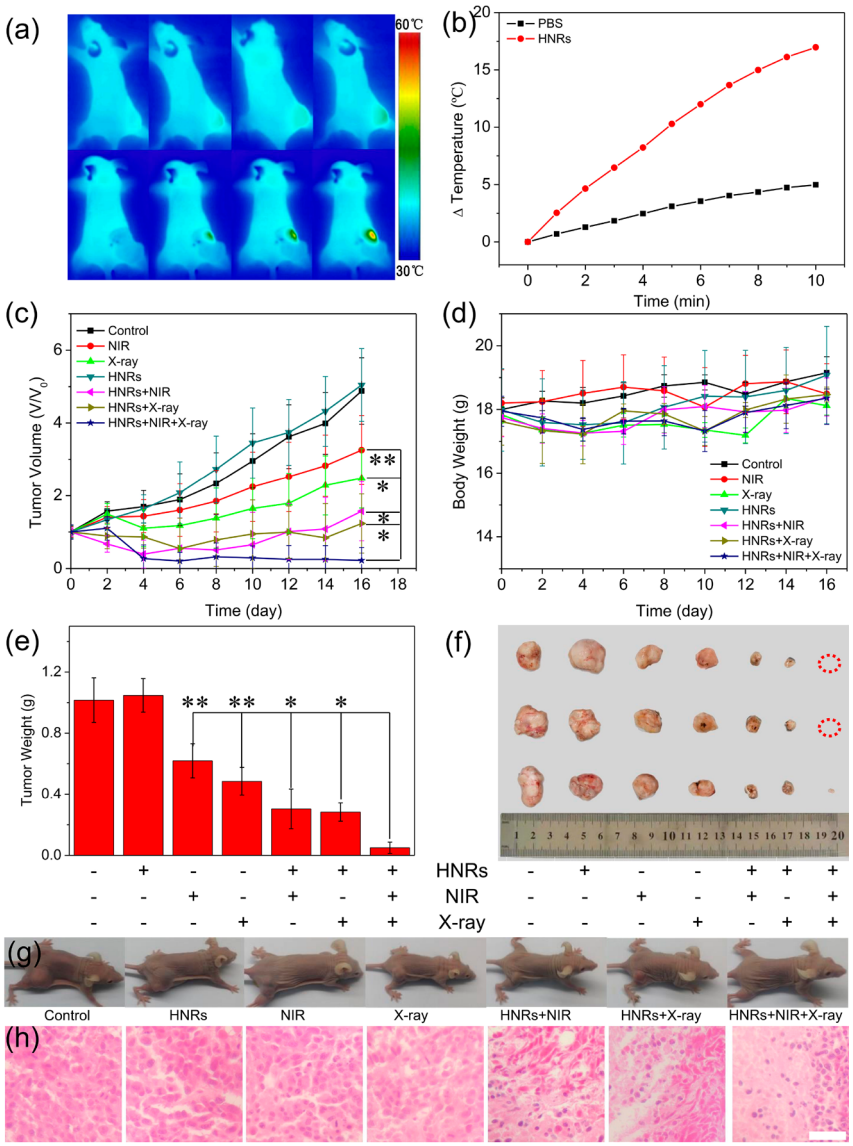

Figure 7. (a) Infrared imaging photographs of KB tumor-bearing mice with injection of PBS or $BiVO_4@Bi_2S_3$ HNRs (laser, 808 nm; 0.33 W/cm^2). (b) Temperature rising curves of tumors during NIR laser irradiation. (c, d) Tumor volume and body weight curves of mice during 16 days. (e, f) Average weights and photographs of tumors at the end of treatment. (g) Photographs of mice at the end of treatment. (h) H&E staining of tumor at the end of treatment (scale bar is 50 μm). *P*-values were calculated by one-way ANOVA: $^*P < 0.05$, $^{**}P < 0.01$, $^{***}P < 0.001$.

eosin (H&E) staining assays are used to evaluate the therapeutic activity of $BiVO_4@Bi_2S_3$ HNRs. According to the H&E staining images, any kind of single treatment can only induce partial death and nucleus rupture and ablation of tumor cells, whereas the most severe hemorrhagic inflammation and destructive cell necrosis are found in tumor tissues under synergistic therapy. H&E staining assays of major organs and serum biochemistry analysis are further performed to validate the safety of $BiVO_4@Bi_2S_3$ HNRs in vivo treatment (Figures S17−S21). No significant side effect is observed compared to the control group. All the results above are a testament to the excellent biocompatibility and powerful lethality of $BiVO_4@Bi_2S_3$ HNRs during the therapeutic process.

4. CONCLUSION

In summary, we have successfully designed and prepared Tween-20-modified $BiVO_4@Bi_2S_3$ HNRs as a multifunctional nanotheranostic platform for multimodal CT/PA imaging and RT/RDT/PTT synergistic therapy. The as-prepared $BiVO_4@Bi_2S_3$ HNRs exhibit the superior performances in terms of X-ray absorption and photothermal conversion owing to the high X-ray attenuation coefficient of Bi and strong NIR absorption of Bi_2S_3, which strongly guarantee their future applications as photothermal transducers for PA/PTT and radiosensitizers for CT/RT. More importantly, by taking advantage of the type II band alignment between $BiVO_4$ and Bi_2S_3, an extra internal electric field is established to accelerate the separation of X-ray-induced electrons and holes in $BiVO_4@Bi_2S_3$ HNRs, resulting in the realization of high-effective RDT under X-ray irradiation. At last, the in vitro and in vivo studies verify that our $BiVO_4@Bi_2S_3$ HNRs possess no appreciable toxicity but higher RT/RDT/PTT synergistic therapeutic efficacy than any single treatment. Because the preparation of heterojunction nanostructures has been well developed, our work may offer a new point of view on the design and construct of nanomaterials for malignant tumor diagnosis and therapy.

https://dx.doi.org/10.1021/acsabm.0c00573
ACS Appl. Bio Mater. XXXX, XXX, XXX−XXX

■ ASSOCIATED CONTENT

Supporting Information

The Supporting Information is available free of charge at https://pubs.acs.org/doi/10.1021/acsabm.0c00573.

TEM images, photographs, XPS spectra, UPS spectra, EPR spectra, ROS detection spectra, cytotoxicity of $BiVO_4$@Bi_2S_3 HNRs and $BiVO_4$ NRs, H&E stained photographs of organs, and blood analysis results (PDF)

■ AUTHOR INFORMATION

Corresponding Authors

Yi Liu − *State Key Laboratory of Supramolecular Structure and Materials, College of Chemistry, Jilin University, Changchun 130012, People's Republic of China;* orcid.org/0000-0003-0548-6073; Email: yiliuchem@jlu.edu.cn

Yu Chong − *State Key Laboratory of Radiation Medicine and Protection, School for Radiological and Interdisciplinary Sciences (RAD-X), Collaborative Innovation Center of Radiation Medicine of Jiangsu Higher Education Institutions, Soochow University, Suzhou 215123, People's Republic of China;* orcid.org/0000-0002-6538-2498; Email: chongyu@suda.edu.cn

Authors

Ze Wang − *State Key Laboratory of Supramolecular Structure and Materials, College of Chemistry, Jilin University, Changchun 130012, People's Republic of China*

Shuwei Liu − *State Key Laboratory of Supramolecular Structure and Materials, College of Chemistry, Jilin University, Changchun 130012, People's Republic of China*

Lu Wang − *Department of Oral Pathology, School and Hospital of Stomatology, Jilin University, Changchun 130021, People's Republic of China*

Haoyang Zou − *State Key Laboratory of Supramolecular Structure and Materials, College of Chemistry, Jilin University, Changchun 130012, People's Republic of China*

Zidong Wang − *State Key Laboratory of Supramolecular Structure and Materials, College of Chemistry, Jilin University, Changchun 130012, People's Republic of China*

Xiaoduo Tang − *State Key Laboratory of Supramolecular Structure and Materials, College of Chemistry, Jilin University, Changchun 130012, People's Republic of China*

Wenjie Feng − *State Key Laboratory of Supramolecular Structure and Materials, College of Chemistry, Jilin University, Changchun 130012, People's Republic of China*

Bai Yang − *State Key Laboratory of Supramolecular Structure and Materials, College of Chemistry, Jilin University, Changchun 130012, People's Republic of China;* orcid.org/0000-0002-3873-075X

Hao Zhang − *State Key Laboratory of Supramolecular Structure and Materials, College of Chemistry, Jilin University, Changchun 130012, People's Republic of China;* orcid.org/0000-0002-2373-1100

Complete contact information is available at: https://pubs.acs.org/10.1021/acsabm.0c00573

Notes

The authors declare no competing financial interest.

■ ACKNOWLEDGMENTS

This work was supported by NSFC (21875086, 21906110), JLU Science and Technology Innovative Research Team (2017TD-06), the Special Project from MOST of China, and the opening funds of State Key Laboratory of Applied Optics, Changchun Institute of Optics, Fine Mechanics and Physics, Chinese Academy of Science. Y.C. appreciates the support from the Natural Science Foundation of Jiangsu Province (BK20170353).

■ REFERENCES

(1) Siegel, R. L.; Miller, K. D.; Jemal, A. Cancer Statistics, 2019. *Ca-Cancer J. Clin.* **2019**, *69* (1), 7−34.

(2) Goel, S.; Ni, D.; Cai, W. Harnessing the Power of Nanotechnology for Enhanced Radiation Therapy. *ACS Nano* **2017**, *11*, 5233−5237.

(3) Chen, X.; Song, J.; Chen, X.; Yang, H. X-ray-activated Nanosystems for Theranostic Applications. *Chem. Soc. Rev.* **2019**, *48*, 3073−3101.

(4) Atun, R.; Jaffray, D. A.; Barton, M. B.; Bray, F.; Baumann, M.; Vikram, B.; Hanna, T. P.; Knaul, F. M.; Lievens, Y.; Lui, T. Y. M.; Milosevic, M.; O'Sullivan, B.; Rodin, D. L.; Rosenblatt, E.; Van Dyk, J.; Yap, M. L.; Zubizarreta, E.; Gospodarowicz, M. Expanding Global Access to Radiotherapy. *Lancet Oncol.* **2015**, *16*, 1153−1186.

(5) Barker, H. E.; Paget, J. T. E.; Khan, A. A.; Harrington, K. J. The Tumour Microenvironment after Radiotherapy: Mechanisms of Resistance and Recurrence. *Nat. Rev. Cancer* **2015**, *15*, 409−425.

(6) Jiang, W.; Li, Q.; Xiao, L.; Dou, J. X.; Liu, Y.; Yu, W. H.; Ma, Y. C.; Li, X. Q.; You, Y. Z.; Tong, Z. T.; Liu, H.; Liang, H.; Lu, L. G.; Xu, X. D.; Yao, Y. D.; Zhang, G. Q.; Wang, Y. C.; Wang, J. Hierarchical Multiplexing Nanodroplets for Imaging-Guided Cancer Radiotherapy via DNA Damage Enhancement and Concomitant DNA Repair Prevention. *ACS Nano* **2018**, *12*, 5684−5689.

(7) O'Connor, M. J. Targeting the DNA Damage Response in Cancer. *Mol. Cell* **2015**, *60*, 547−560.

(8) Li, Z.; Hu, Y.; Miao, Z.; Xu, H.; Li, C.; Zhao, Y.; Li, Z.; Chang, M.; Ma, Z.; Sun, Y.; Besenbacher, F.; Huang, P.; Yu, M. Dual-Stimuli Responsive Bismuth Nanoraspberries for Multimodal Imaging and Combined Cancer Therapy. *Nano Lett.* **2018**, *18*, 6778−6788.

(9) Siddiqui, M. S.; Francois, M.; Fenech, M. F.; Leifert, W. R. Persistent Gamma H2AX: A Promising Molecular Marker of DNA Damage and Aging. *Mutat. Res., Rev. Mutat. Res.* **2015**, *766*, 1−19.

(10) Fan, W.; Bu, W.; Zhang, Z.; Shen, B.; Zhang, H.; He, Q.; Ni, D.; Cui, Z.; Zhao, K.; Bu, J.; Du, J.; Liu, J.; Shi, J. X-ray Radiation-Controlled NO-Release for On-Demand Depth-Independent Hypoxic Radiosensitization. *Angew. Chem., Int. Ed.* **2015**, *54*, 14026−14030.

(11) Begg, A. C.; Stewart, F. A.; Vens, C. Strategies to Improve Radiotherapy with Targeted Drugs. *Nat. Rev. Cancer* **2011**, *11*, 239−253.

(12) Li, L.; Lu, Y.; Jiang, C.; Zhu, Y.; Yang, X.; Hu, X.; Lin, Z.; Zhang, Y.; Peng, M.; Xia, H.; Mao, C. Actively Targeted Deep Tissue Imaging and Photothermal-Chemo Therapy of Breast Cancer by Antibody-Functionalized Drug-Loaded X-Ray-Responsive Bismuth Sulfide@Mesoporous Silica Core-Shell Nanoparticles. *Adv. Funct. Mater.* **2018**, *28*, 1704623.

(13) Li, L.; Lu, Y.; Lin, Z.; Mao, A. S.; Jiao, J.; Zhu, Y.; Jiang, C.; Yang, Z.; Peng, M.; Mao, C. Ultralong tumor retention of theranostic nanoparticles with short peptide-enabled active tumor homing. *Mater. Horiz.* **2019**, *6*, 1845−1853.

(14) Wang, H.; Mu, X. Y.; He, H.; Zhang, X. D. Cancer Radiosensitizers. *Trends Pharmacol. Sci.* **2018**, *39*, 24−48.

(15) Goswami, N.; Luo, Z. T.; Yuan, X.; Leong, D. T.; Xie, J. P. Engineering Gold-based Tadiosensitizers for Cancer Radiotherapy. *Mater. Horiz.* **2017**, *4*, 817−831.

(16) Zhou, R.; Wang, H.; Yang, Y.; Zhang, C.; Dong, X.; Du, J.; Yan, L.; Zhang, G.; Gu, Z.; Zhao, Y. Tumor microenvironment-manipulated radiocatalytic sensitizer based on bismuth heteropoly-tungstate for radiotherapy enhancement. *Biomaterials* **2019**, *189*, 11−22.

(17) Her, S.; Jaffray, D. A.; Allen, C. Gold Nanoparticles for Applications in Cancer Radiotherapy: Mechanisms and Recent Advancements. *Adv. Drug Delivery Rev.* **2017**, *109*, 84−101.
(18) Luo, D.; Wang, X.; Zeng, S.; Ramamurthy, G.; Burda, C.; Basilion, J. P. Targeted Gold Nanocluster-Enhanced Radiotherapy of Prostate Cancer. *Small* **2019**, *15*, 1900968.
(19) Liu, J.; Zheng, X.; Yan, L.; Zhou, L.; Tian, G.; Yin, W.; Wang, L.; Liu, Y.; Hu, Z.; Gu, Z.; Chen, C.; Zhao, Y. Bismuth Sulfide Nanorods as a Precision Nanomedicine for in Vivo Multimodal Imaging-Guided Photothermal Therapy of Tumor. *ACS Nano* **2015**, *9*, 696−707.
(20) Wang, Y.; Wu, Y.; Liu, Y.; Shen, J.; Lv, L.; Li, L.; Yang, L.; Zeng, J.; Wang, Y.; Zhang, L. W.; Li, Z.; Gao, M.; Chai, Z. BSA-Mediated Synthesis of Bismuth Sulfide Nanotheranostic Agents for Tumor Multimodal Imaging and Thermoradiotherapy. *Adv. Funct. Mater.* **2016**, *26*, 5335−5344.
(21) Yu, X.; Liu, X.; Wu, W.; Yang, K.; Mao, R.; Ahmad, F.; Chen, X.; Li, W. Computed Tomography and Magnetic Resonance Imaging-Guided Synergistic Radiotherapy and X-ray Inducible Photodynamic Therapy Using Tb-Doped Gadolinium Tungstate Nanoscintillators. *Angew. Chem., Int. Ed.* **2019**, *58*, 2017−2022.
(22) Hu, X.; Sun, J.; Li, F.; Li, R.; Wu, J.; He, J.; Wang, N.; Liu, J.; Wang, S.; Zhou, F.; Sun, X.; Kim, D.; Hyeon, T.; Ling, D. Renal-Clearable Hollow Bismuth Subcarbonate Nanotubes for Tumor Targeted Computed Tomography Imaging and Chemoradiotherapy. *Nano Lett.* **2018**, *18*, 1196−1204.
(23) Yu, X.; Li, A.; Zhao, C.; Yang, K.; Chen, X.; Li, W. Ultrasmall Semimetal Nanoparticles of Bismuth for Dual-Modal Computed Tomography/Photoacoustic Imaging and Synergistic Thermoradiotherapy. *ACS Nano* **2017**, *11*, 3990−4001.
(24) Malfertheiner, P.; Bazzoli, F.; Delchier, J. C.; Celinski, K.; Giguere, M.; Riviere, M.; Megraud, F. Helicobacter Pylori Eradication with a Capsule Containing Bismuth Subcitrate Potassium, Metronidazole, and Tetracycline Given with Omeprazole Versus Clarithromycin-Based Triple Therapy: A Randomised, Open-label, Non-inferiority, Phase 3. *Lancet* **2011**, *377*, 905−913.
(25) Sun, Q. J.; Liang, X.; Zheng, Q.; Liu, W. Z.; Xiao, S. D.; Gu, W. Q.; Lu, H. High Efficacy of 14-Day Triple Therapy-Based, Bismuth-Containing Quadruple Therapy for Initial Helicobacter Pylori Eradication. *Helicobacter* **2010**, *15*, 233−238.
(26) Wang, G. D.; Nguyen, H. T.; Chen, H.; Cox, P. B.; Wang, L.; Nagata, K.; Hao, Z.; Wang, A.; Li, Z.; Xie, J. X-Ray Induced Photodynamic Therapy: A Combination of Radiotherapy and Photodynamic Therapy. *Theranostics* **2016**, *6*, 2295−2305.
(27) Larue, L.; Ben Mihoub, A.; Youssef, Z.; Colombeau, L.; Acherar, S.; Andre, J. C.; Arnoux, P.; Baros, F.; Vermandel, M.; Frochot, C. Using X-rays in Photodynamic Therapy: an Overview. *Photochem. Photobiol. Sci.* **2018**, *17*, 1612−1650.
(28) Kamkaew, A.; Chen, F.; Zhan, Y.; Majewski, R. L.; Cai, W. Scintillating Nanoparticles as Energy Mediators for Enhanced Photodynamic Therapy. *ACS Nano* **2016**, *10*, 3918−3935.
(29) Ni, K. Y.; Lan, G. X.; Veroneau, S. S.; Duan, X. P.; Song, Y.; Lin, W. B. Nanoscale Metal-Organic Frameworks for Mitochondria-Targeted Radiotherapy-Radiodynamic Therapy. *Nat. Commun.* **2018**, *9*, 4321.
(30) Lu, K. D.; He, C. B.; Guo, N. N.; Chan, C.; Ni, K. Y.; Lan, G. X.; Tang, H. D.; Pelizzari, C.; Fu, Y. X.; Spiotto, M. T.; Weichselbaum, R. R.; Lin, W. B. Low-dose X-ray Radiotherapy-Radiodynamic Therapy via Nanoscale Metal-Organic Frameworks Enhances Checkpoint Blockade Immunotherapy. *Nat. Biomed. Eng.* **2018**, *2*, 600−610.
(31) Agostinis, P.; Berg, K.; Cengel, K. A.; Foster, T. H.; Girotti, A. W.; Gollnick, S. O.; Hahn, S. M.; Hamblin, M. R.; Juzeniene, A.; Kessel, D.; Korbelik, M.; Moan, J.; Mroz, P.; Nowis, D.; Piette, J.; Wilson, B. C.; Golab, J. Photodynamic Therapy of Cancer: An Update. *Ca-Cancer J. Clin.* **2011**, *61*, 250−281.
(32) Han, K.; Zhang, J.; Zhang, W.; Wang, S.; Xu, L.; Zhang, C.; Zhang, X.; Han, H. Tumor-Triggered Geometrical Shape Switch of Chimeric Peptide for Enhanced in Vivo Tumor Internalization and Photodynamic Therapy. *ACS Nano* **2017**, *11*, 3178−3188.
(33) Wang, H.; Lv, B.; Tang, Z.; Zhang, M.; Ge, W.; Liu, Y.; He, X.; Zhao, K.; Zheng, X.; He, M.; Bu, W. Scintillator-based Nanohybrids with Sacrificial Electron Prodrug for Enhanced X-ray-induced Photodynamic Therapy. *Nano Lett.* **2018**, *18*, 5768−5774.
(34) Zhang, C.; Zhao, K.; Bu, W.; Ni, D.; Liu, Y.; Feng, J.; Shi, J. Marriage of Scintillator and Semiconductor for Synchronous Radiotherapy and Deep Photodynamic Therapy with Diminished Oxygen Dependence. *Angew. Chem., Int. Ed.* **2015**, *54*, 1770−1774.
(35) Zhong, X.; Wang, X.; Zhan, G.; Tang, Y.; Yao, Y.; Dong, Z.; Hou, L.; Zhao, H.; Zeng, S.; Hu, J.; Cheng, L.; Yang, X. $NaCeF_4$:Gd,Tb Scintillator as X-ray Responsive Photosensitizer for Multimodal Imaging-Guided Synchronous Radio/Radiodynamic Therapy. *Nano Lett.* **2019**, *19*, 8234−8244.
(36) Sahu, S. P.; Cates, E. L. X ray Radiocatalytic Activity and Mechanisms of Bismuth Complex Oxides. *J. Phys. Chem. C* **2017**, *121*, 10538−10545.
(37) Guo, Z.; Zhu, S.; Yong, Y.; Zhang, X.; Dong, X.; Du, J.; Xie, J.; Wang, Q.; Gu, Z.; Zhao, Y. Synthesis of BSA-Coated BiOI@Bi_2S_3 Semiconductor Heterojunction Nanoparticles and Their Applications for Radio/Photodynamic/Photothermal Synergistic Therapy of Tumor. *Adv. Mater.* **2017**, *29*, 1704136.
(38) Song, G.; Liang, C.; Gong, H.; Li, M.; Zheng, X.; Cheng, L.; Yang, K.; Jiang, X.; Liu, Z. Core-Shell MnSe@Bi_2Se_3 Fabricated via a Cation Exchange Method as Novel Nanotheranostics for Multimodal Imaging and Synergistic Thermoradiotherapy. *Adv. Mater.* **2015**, *27*, 6110−6117.
(39) Zhao, P.; Liu, S.; Wang, L.; Liu, G.; Cheng, Y.; Lin, M.; Sui, K.; Zhang, H. Alginate mediated functional aggregation of gold nanoclusters for systemic photothermal therapy and efficient renal clearance. *Carbohydr. Polym.* **2020**, *241*, 116344.
(40) Liu, S.; Wang, L.; Zhang, M.; Tao, K.; Wang, B.; Lin, M.; Zhang, X.; Liu, Y.; Hou, Y.; Zhang, H.; Yang, B. Tumor Microenvironment-Responsive Nanoshuttles with Sodium Citrate Modification for Hierarchical Targeting and Improved Tumor Theranostics. *ACS Appl. Mater. Interfaces* **2019**, *11*, 25730−25739.
(41) Cheng, Y.; Liu, S.; Wang, L.; Liu, G.; Zhao, P.; Lin, M.; Sui, K.; Zhang, H. Homologous cancerous cell membrane modulated multifunctional nanoshuttles: Targeting specificity and improved tumor theranostics. *Compos. Commun.* **2020**, *20*, 100342.
(42) Song, G.; Liang, C.; Yi, X.; Zhao, Q.; Cheng, L.; Yang, K.; Liu, Z. Perfluorocarbon-Loaded Hollow Bi_2Se_3 Nanoparticles for Timely Supply of Oxygen under Near-Infrared Light to Enhance the Radiotherapy of Cancer. *Adv. Mater.* **2016**, *28*, 2716−2723.
(43) Liu, Y.; Ai, K.; Lu, L. Nanoparticulate X ray Computed Tomography Contrast Agents: From Design Validation to in Vivo Applications. *Acc. Chem. Res.* **2012**, *45*, 1817−1827.
(44) Ai, K.; Liu, Y.; Liu, J.; Yuan, Q.; He, Y.; Lu, L. Large-Scale Synthesis of Bi_2S_3 Nanodots as a Contrast Agent for In Vivo X-ray Computed Tomography Imaging. *Adv. Mater.* **2011**, *23*, 4886−4891.
(45) Wang, L. V.; Hu, S. Photoacoustic Tomography: In Vivo Imaging from Organelles to Organs. *Science* **2012**, *335*, 1458−1462.
(46) Liu, Y.; He, J.; Yang, K.; Yi, C.; Liu, Y.; Nie, L.; Khashab, N. M.; Chen, X.; Nie, Z. Folding Up of Gold Nanoparticle Strings into Plasmonic Vesicles for Enhanced Photoacoustic Imaging. *Angew. Chem., Int. Ed.* **2015**, *54*, 15809−15812.
(47) Chauhan, V. P.; Popović, Z.; Chen, O.; Cui, J.; Fukumura, D.; Bawendi, M. G.; Jain, R. K. Fluorescent Nanorods and Nanospheres for Real-Time In Vivo Probing of Nanoparticle Shape-Dependent Tumor Penetration. *Angew. Chem., Int. Ed.* **2011**, *50*, 11417−11420.
(48) Kolhar, P.; Doshi, N.; Mitragotri, S. Polymer Nanoneedle-Mediated Intracellular Drug Delivery. *Small* **2011**, *7*, 2094−2100.
(49) Barreto, J. A.; O'Malley, W.; Kubeil, M.; Graham, B.; Stephan, H.; Spiccia, L. Nanomaterials: Applications in Cancer Imaging and Therapy. *Adv. Mater.* **2011**, *23*, H18−40.
(50) Shichibu, Y.; Negishi, Y.; Tsunoyama, H.; Kanehara, M.; Teranishi, T.; Tsukuda, T. Extremely High Stability of Glutathionate-

https://dx.doi.org/10.1021/acsabm.0c00573
ACS Appl. Bio Mater. XXXX, XXX, XXX−XXX

Protected Au_{25} Clusters Against Core Etching. *Small* **2007**, *3*, 835−839.
(51) Szychowski, B.; Leng, H.; Pelton, M.; Daniel, M. Controlled etching and tapering of Au nanorods using cysteamine. *Nanoscale* **2018**, *10*, 16830−16838.
(52) Xuan, Y.; Yang, X.; Song, Z.; Zhang, R.; Zhao, D.; Hou, X.; Song, X.; Liu, B.; Zhao, Y.; Chen, W. High-Security Multifunctional Nano-Bismuth-Sphere-Cluster Prepared from Oral Gastric Drug for CT/PA Dual-Mode Imaging and Chemo-Photothermal Combined Therapy In Vivo. *Adv. Funct. Mater.* **2019**, *29*, 1900017.
(53) Liu, Y.; Tang, Y.; Ning, Y.; Li, M.; Zhang, H.; Yang, B. One-pot" Synthesis and Shape Control of ZnSe Semiconductor Nanocrystals in Liquid Paraffin. *J. Mater. Chem.* **2010**, *20*, 4451−4458.
(54) Dong, C.; Lu, S.; Yao, S.; Ge, R.; Wang, Z.; Wang, Z.; An, P.; Liu, Y.; Yang, B.; Zhang, H. Colloidal Synthesis of Ultrathin Monoclinic $BiVO_4$ Nanosheets for Z-Scheme Overall Water Splitting under Visible Light. *ACS Catal.* **2018**, *8*, 8649−8658.
(55) Wang, X.; Zhang, C.; Du, J.; Dong, X.; Jian, S.; Yan, L.; Gu, Z.; Zhao, Y. Enhanced Generation of Non-Oxygen Dependent Free Radicals by Schottky-type Heterostructures of Au−Bi_2S_3 Nanoparticles via X-ray-Induced Catalytic Reaction for Radiosensitization. *ACS Nano* **2019**, *13*, 5947−5958.
(56) Nosaka, Y.; Nosaka, A. Y. Generation and Detection of Reactive Oxygen Species in Photocatalysis. *Chem. Rev.* **2017**, *117*, 11302−11336.
(57) Schweitzer, C.; Schmidt, R. Physical Mechanisms of Generation and Deactivation of Singlet Oxygen. *Chem. Rev.* **2003**, *103*, 1685−1757.
(58) Smith, A. M.; Nie, S. Semiconductor Nanocrystals: Structure, Properties, and Band Gap Engineering. *Acc. Chem. Res.* **2010**, *43*, 190−200.
(59) Wang, S.; Hai, X.; Ding, X.; Chang, K.; Xiang, Y.; Meng, X.; Yang, Z.; Chen, H.; Ye, J. Light-Switchable Oxygen Vacancies in Ultrafne Bi_5O_7Br Nanotubes for Boosting Solar-Driven Nitrogen Fixation in Pure Water. *Adv. Mater.* **2017**, *29*, 1701774.
(60) Li, H.; Shang, J.; Ai, Z.; Zhang, L. Efficient Visible Light Nitrogen Fixation with BiOBr Nanosheets of Oxygen Vacancies on the Exposed {001} Facets. *J. Am. Chem. Soc.* **2015**, *137*, 6393−6399.
(61) Wang, G.; Wang, H.; Ling, Y.; Tang, Y.; Yang, X.; Fitzmorris, R. C.; Wang, C.; Zhang, J. Z.; Li, Y. Hydrogen-Treated TiO_2 Nanowire Arrays for Photoelectrochemical Water Splitting. *Nano Lett.* **2011**, *11*, 3026−3033.
(62) Xiao, L.; Gu, L.; Howell, S. B.; Sailor, M. J. Porous Silicon Nanoparticle Photosensitizers for Singlet Oxygen and Their Phototoxicity against Cancer Cells. *ACS Nano* **2011**, *5*, 3651−3659.
(63) Huang, Y.; Kang, S.; Yang, Y.; Qin, H.; Ni, Z.; Yang, S.; Li, X. Facile synthesis of Bi/Bi_2WO_6 nanocomposite with enhanced photocatalytic activity under visible light. *Appl. Catal., B* **2016**, *196*, 89−99.
(64) Heinrich, M. C.; Haberle, L.; Muller, V.; Bautz, W.; Uder, M. Nephrotoxicity of Iso-osmolar Iodixanol Compared with Nonionic Low-osmolar Contrast Media: Meta-analysis of Randomized Controlled Trials. *Radiology* **2009**, *250*, 68−86.
(65) Evgeniy, E.; Sergei, K. Identification of ROS using oxidized DCFDA and flow-cytometry. In *Advanced Protocols in Oxidative Stress II*; Methods in Moecular Biology; Springer, 2010; Vol. *594*, pp 57−72.
(66) Mah, L. J.; El-Osta, A.; Karagiannis, T. C. Gamma H2AX: A Sensitive Molecular Marker of DNA Damage and Repair. *Leukemia* **2010**, *24*, 679−686.

https://dx.doi.org/10.1021/acsabm.0c00573
ACS Appl. Bio Mater. XXXX, XXX, XXX−XXX